Supporting Information

A single fluorescent chemosensor for multiple targets: the sequential detection of Al^{3+} and pyrophosphate and the selective detection of F^- in a near-perfect aqueous solution

Suh Mi Hwang,[a] Min Seon Kim, [a] Misun Lee,[b] Mi Hee Lim,[b]* Cheal Kim[a]*

[a] *Department of Fine Chemistry and Department of Interdisciplinary Bio IT Materials, Seoul National University of Science and Technology, Seoul 139-743, Korea. Fax: +82-2-973-9149; Tel: +82-2-970-6693; E-mail: chealkim@seoultech.ac.kr*

[b] *Department of Chemistry, Ulsan National Institute of Science and Technology (UNIST), Ulsan 44919, Republic of Korea. Fax: +82-52-217-5409; Tel: +82-52-217-5422; E-mail: mhlim@unist.ac.kr*

Table S1. Examples of chemosensors for sequential detection of Al^{3+} and PPi.

Sensor	Limit of detection (Al^{3+}/PPi, μM)	Binding constant (Al^{3+}/PPi, M^{-1})	Percent of water in solution (%)	Method of detection Al^{3+}/PPi	Reference
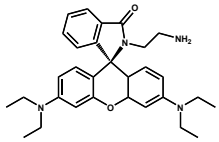	No data / 7.3	1.66 x 10^4 / No data	100	Fluorescence, Colorimetric	[1]
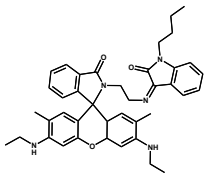	0.86 / 2.19	8.00 x 10^4 / No data	30	Colorimetric	[2]
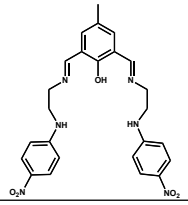	7.55 / 3.34	5.29 ± 1.11 x 10^4 / 1.34 ± 0.81 x 10^3	20	Fluorescence, Colorimetric	[3]
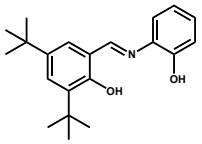	0.03 / 0.27	5.96 x 10^3 / No data	99	Fluorescence	[4]
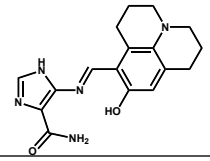	9.24 / 20.5	2.30 x 10^2 / 3.70 x 10^2	99	Fluorescence	[5]
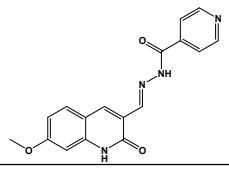	5.6 x 10^{-4} / 0.014	6.95 x 10^2 / No data	100	Fluorescence	[6]
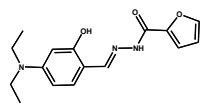	0.185 / 1.20	4.30 x 10^5 / 4.80 x 10^6	99	Fluorescence	This work

References

1 C. R. Lohani, J. M. Kim, S. Y. Chung, J. Y. Yoon and K. H. Lee, *Analyst,* 2010, **135**, 2079–2084.

2 S. Goswami, S. Paul and A. Manna, *RSC adv.,* 2013, **3**, 10639–10643.

3 R. Alam, T. Mistri, R. Bhowmick, A. Katarkar, K. Chaudhuri and M. Ali, *RSC Adv.,* 2015, **5**,

53940-53948.
4 C. Liang, W. Bu, C. Li, G. Men, M. Deng, Y. Jiangyao, H. Sun and S. Jiang, *Dalton Trans.,* 2015, **44**, 11352-11359.
5 T. G. Jo, K. H. Bok, J. Y. Han, M. H. Lim and C. Kim, *Dyes Pigm.,* 2017, **139**, 136-147.
6 S. K. Asthana, A. Kumar, Neeraj, Shweta, S. K. Hira, P. P. Manna and K. K. Upadhyay, *Inorg. Chem.,* 2017, **56**, 3315-3323.

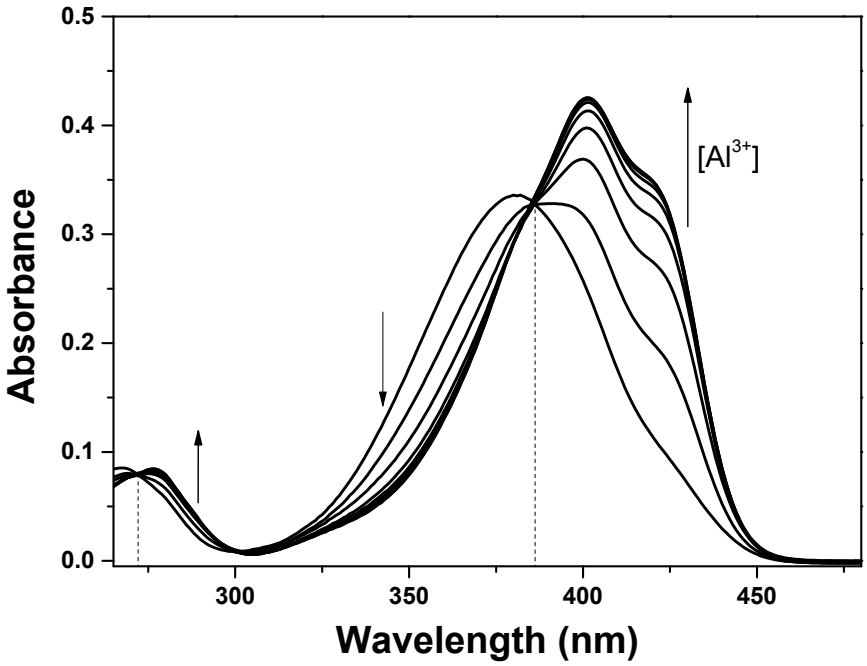

Figure S1. UV-vis titration of **1** (10 μM) with Al^{3+} (up to 4.0 equiv) in bis-tris buffer solution at room temperature.

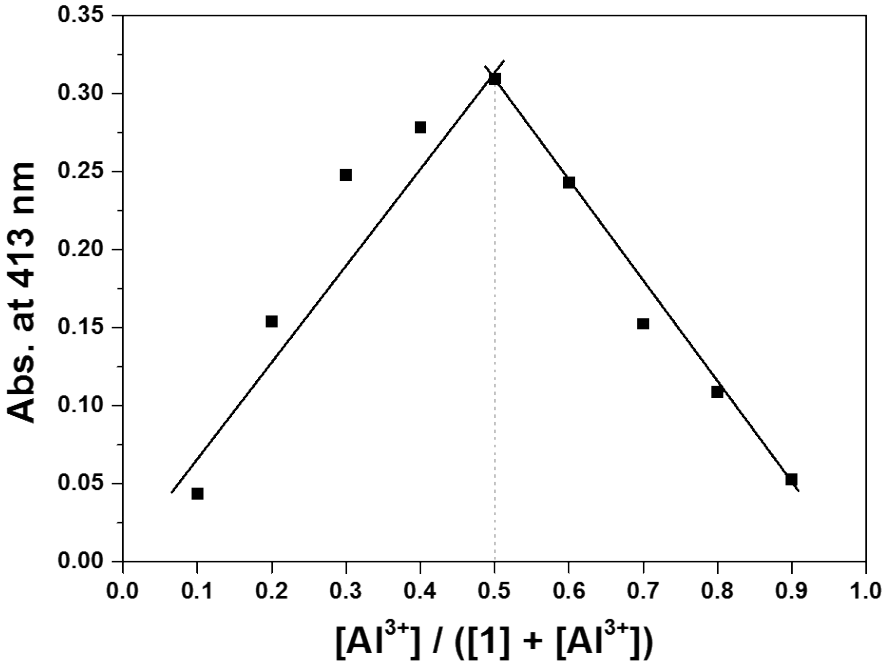

Figure S2. Job plot for the binding of **1** with Al^{3+}. Absorption at 413 nm was plotted as a function of the molar ratio $[Al^{3+}]$ / ([**1**] + $[Al^{3+}]$). The total concentration of Al^{3+} with **1** was 50 μM.

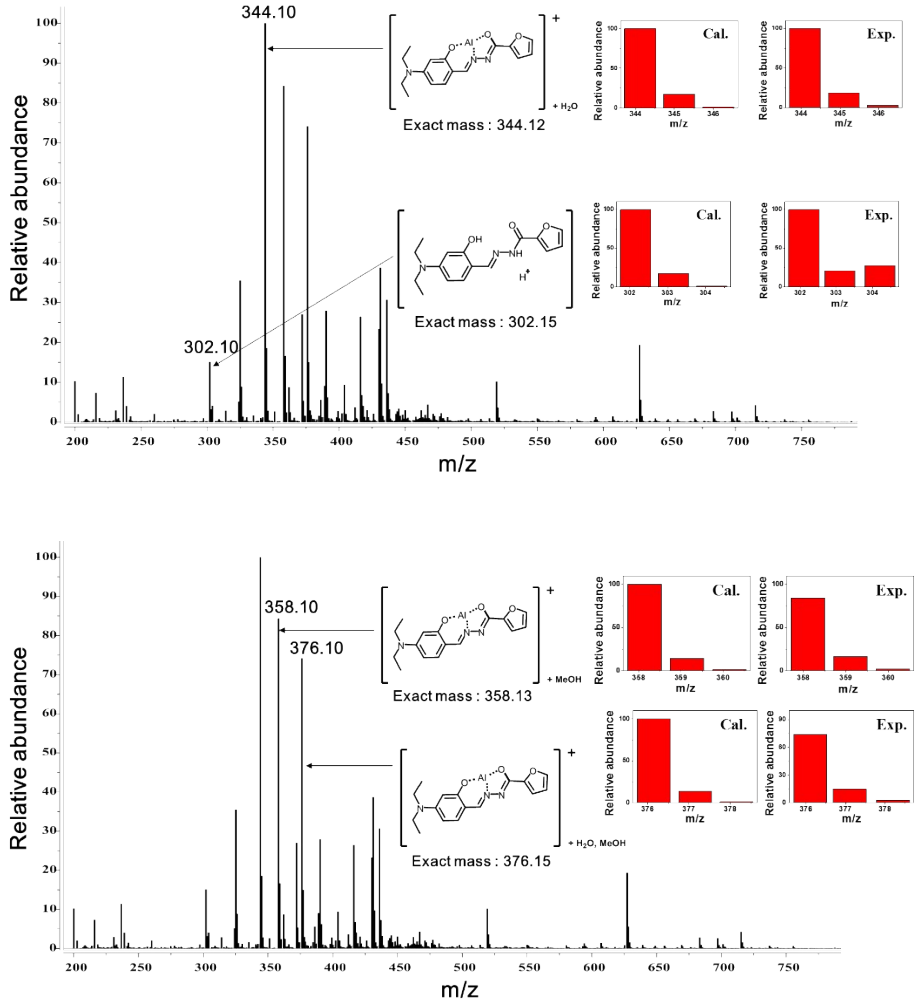

Figure S3. Positive-ion ESI-mass spectrum of **1** (100 μM) upon addition of 1 equiv of Al^{3+}.

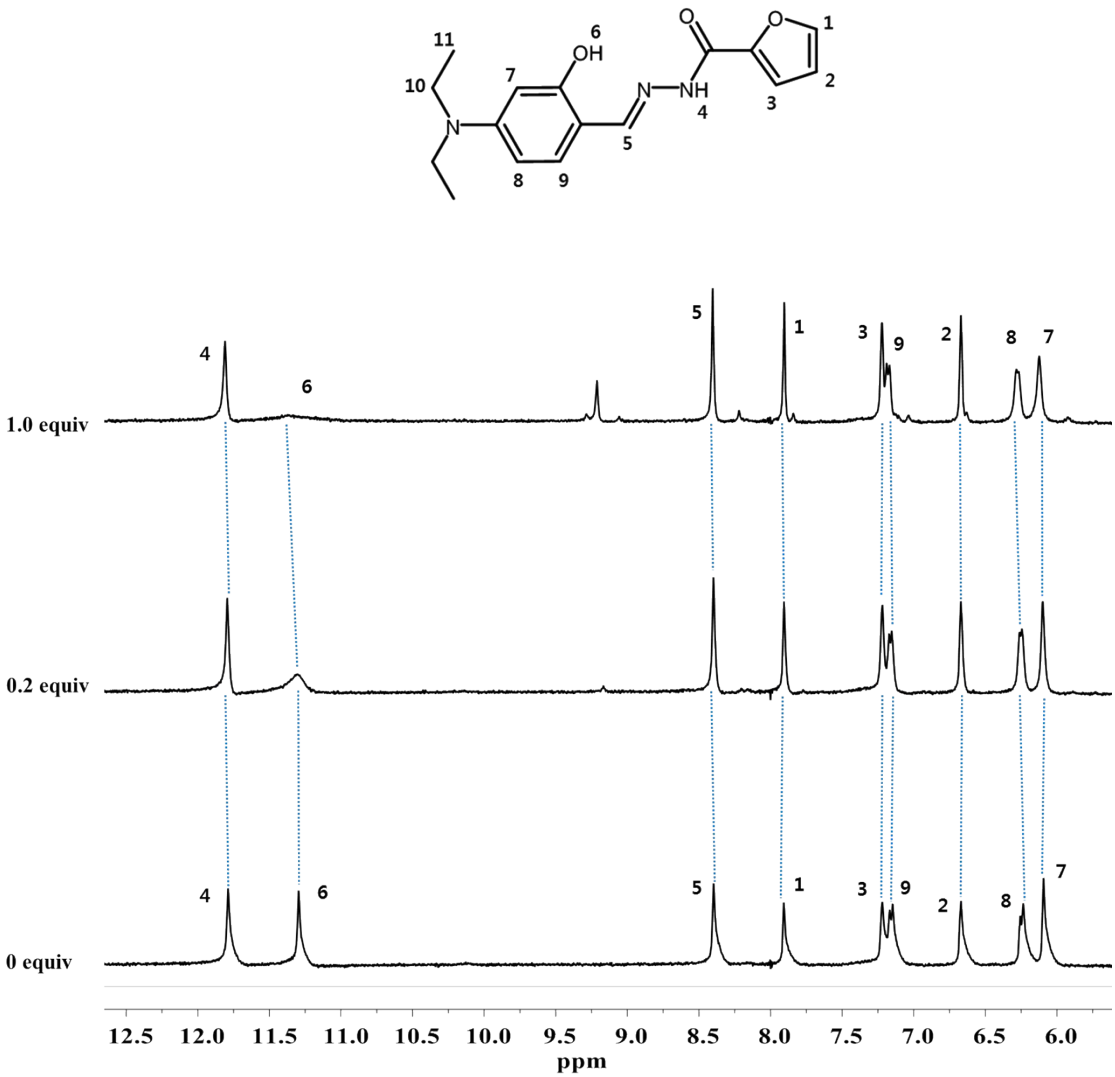

Figure S4. ^{1}H NMR titrations of **1** with Al^{3+}.

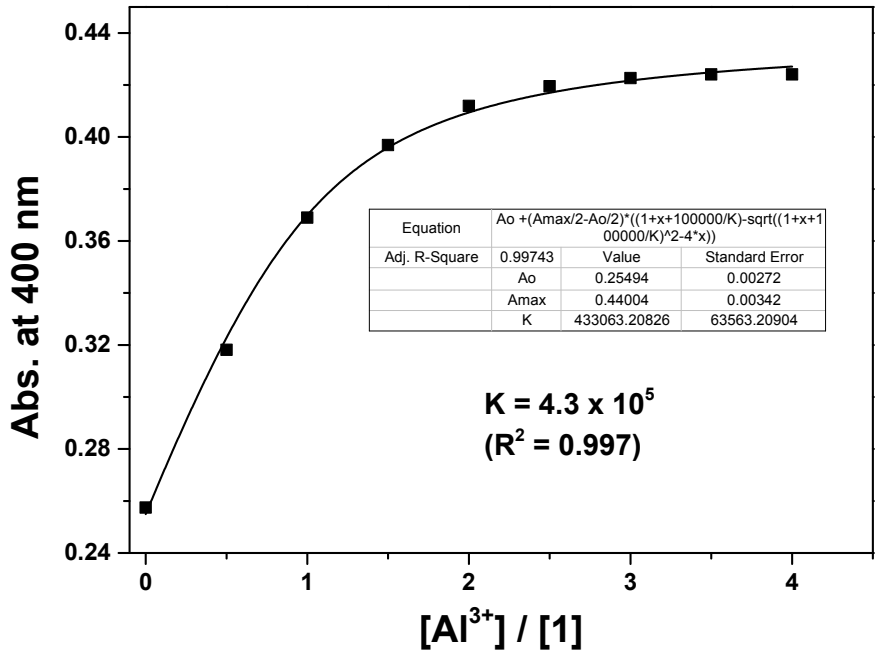

Figure S5. Absorption intensity (at 400 nm) of **1** (10 μM) after addition of increasing different concentration of Al^{3+} ions. The black line is the non-linear fitting curve between **1** and Al^{3+}. Association constant (*K*) of **1** with Al^{3+} was calculated by the non-linear least square curve fitting.

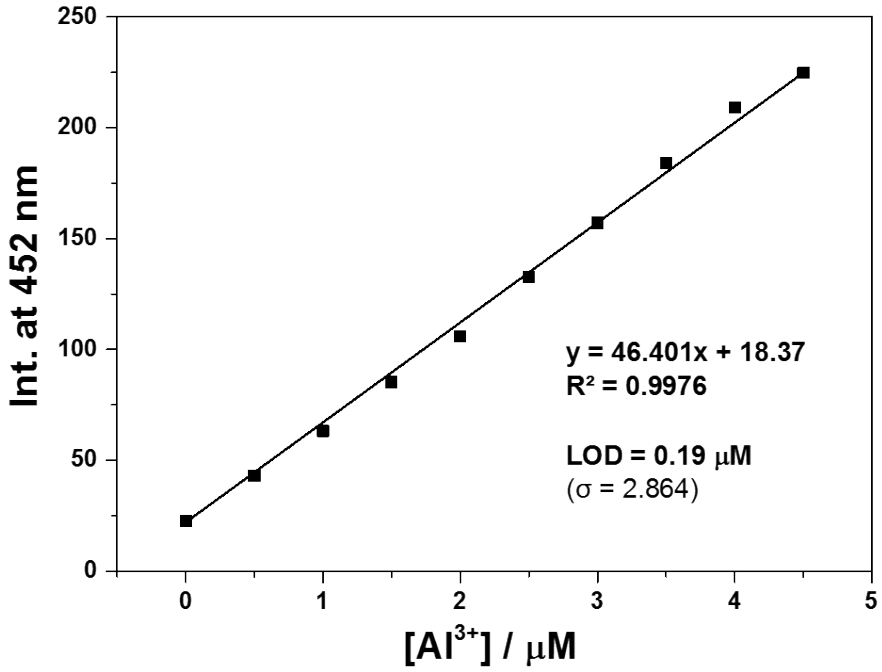

Figure S6. Determination of the limit of detection based on change in the ratio (fluorescence intensity at 452 nm) of **1** with Al^{3+}. [**1**] = 1 μM and [Al^{3+}] = 0-4.5 μM

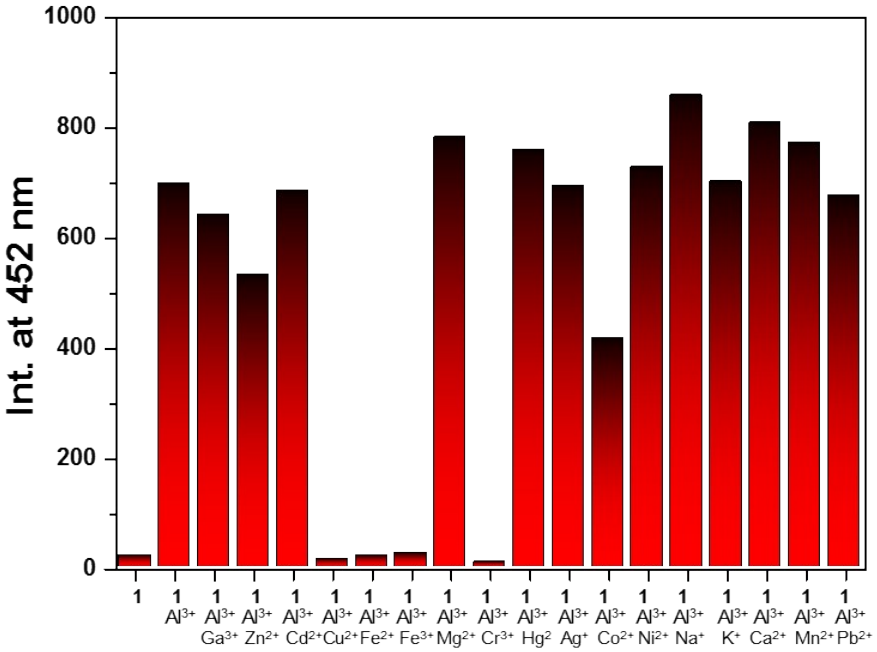

Figure S7. Competitive selectivity of **1 (**1 μM) toward Al^{3+} (24 equiv) in the presence of other metal ions (24 equiv) in bis-tris buffer solution.

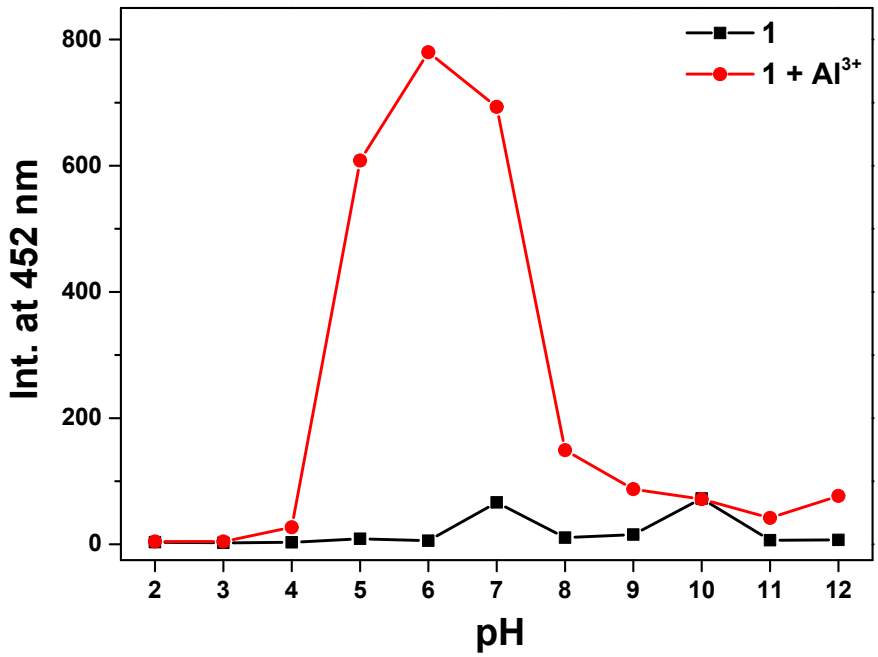

Figure S8. Fluorescence intensities (at 452 nm) of **1** and **1**-Al^{3+} ([**1**] = 1 μM) after addition of 24 equiv of Al^{3+} at various ranges of pH in bis-tris buffer solution.

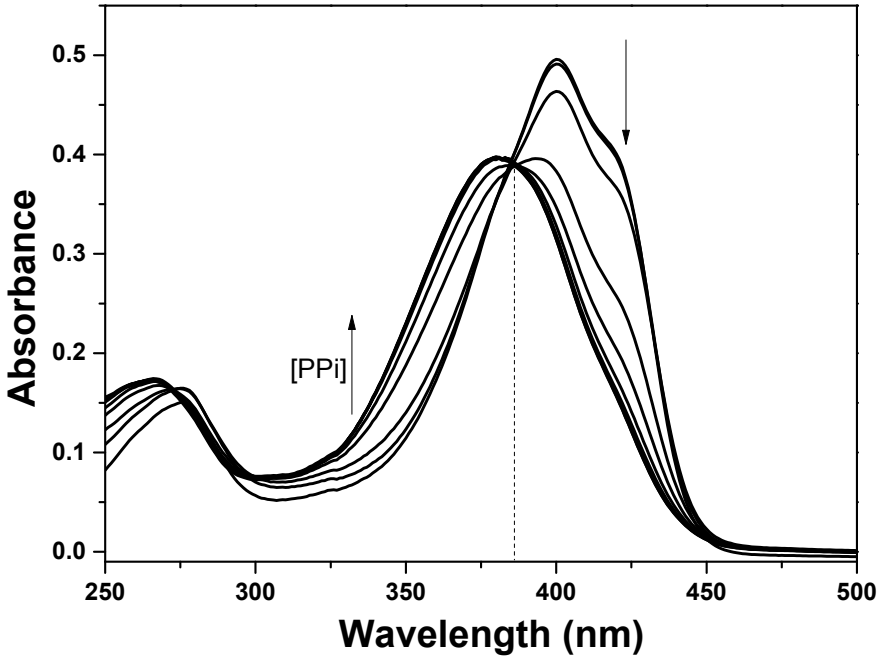

Figure S9. UV-vis titration of **1**-Al^{3+} complex (10 μM) with PPi (up to 18 equiv) in bis-tris buffer solution at room temperature.

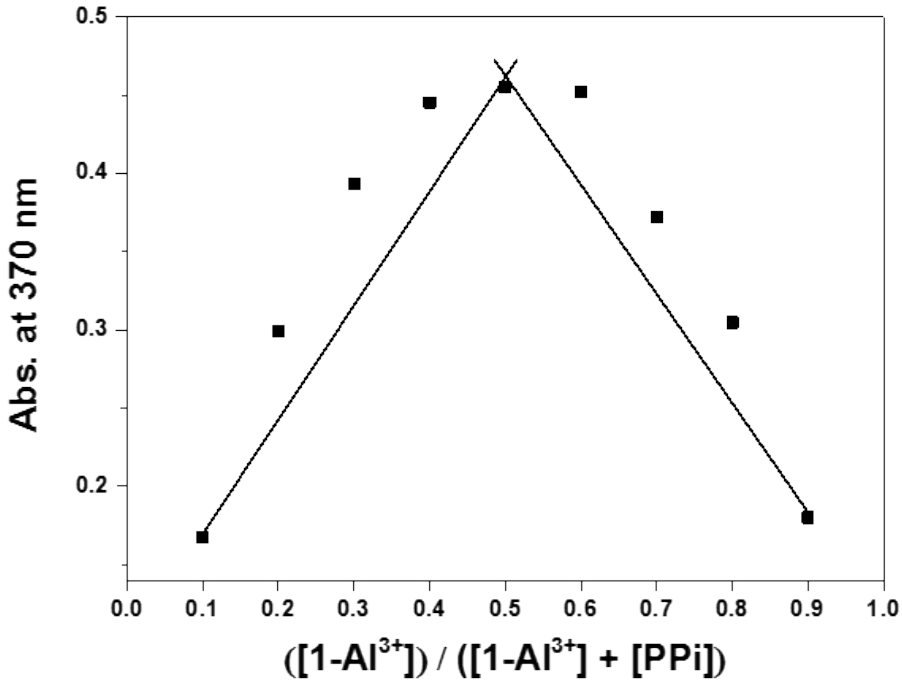

Figure S10. Job plot for the binding of **1**-Al^{3+} complex with PPi. Absorbtion at 370 nm was plotted as a function of the molar ratio ([**1**-Al^{3+}]) / ([**1**-Al^{3+}] + [PPi]). The total concentration of **1**-Al^{3+} complex with PPi was 50 μM.

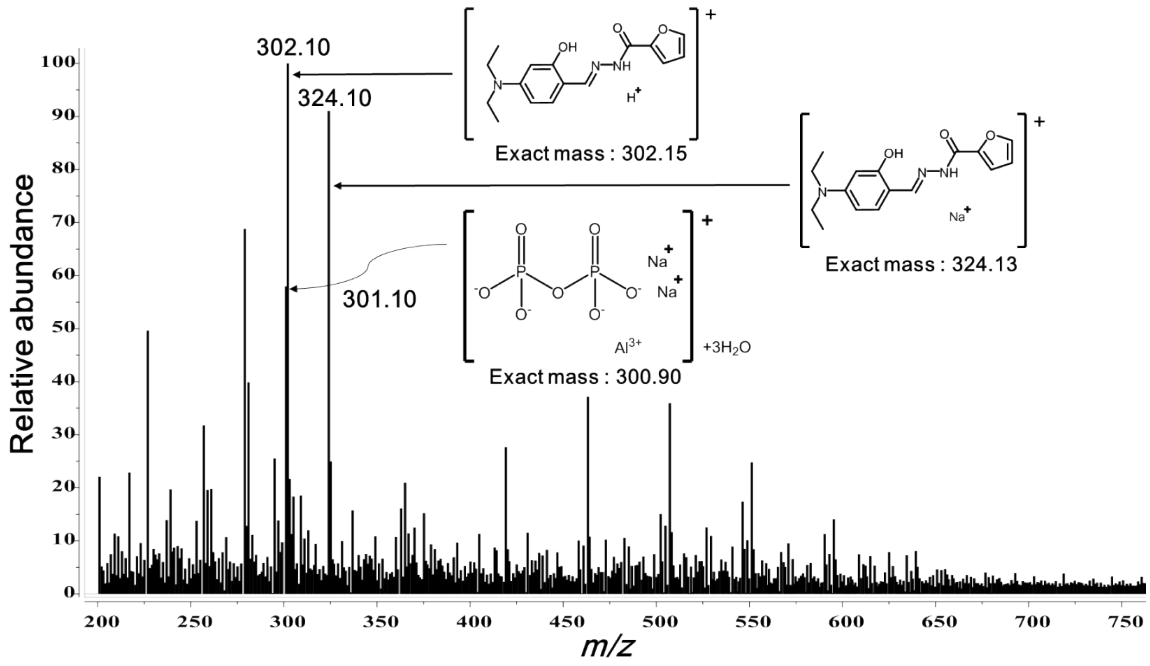

Figure S11. Positive-ion ESI-mass spectrum of **1**-Al^{3+} complex (100 μM) upon addition of 1 equiv of PPi.

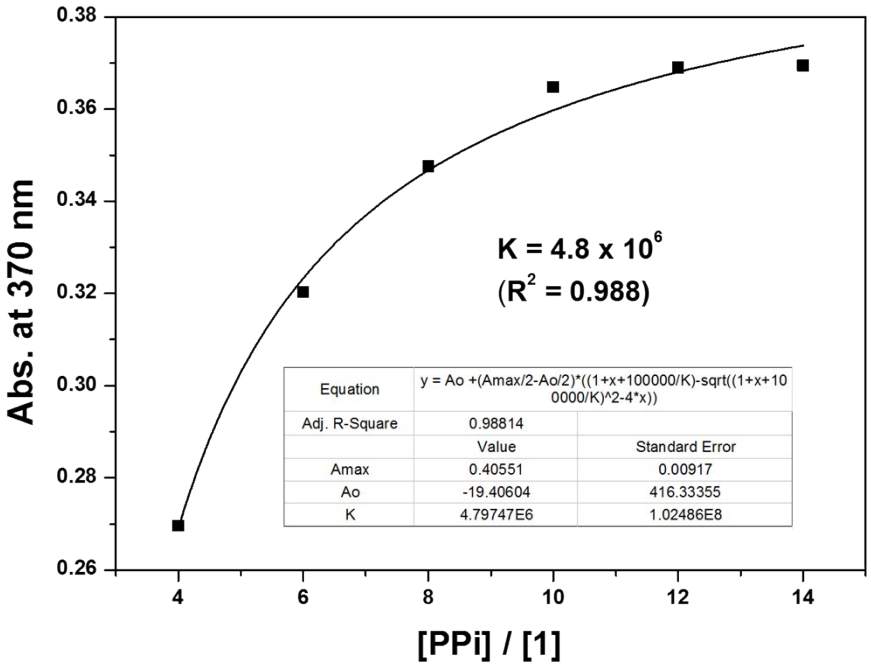

Figure S12. Absorption intensity (at 400 nm) of **1**-Al^{3+} (10 μM) after addition of increasing different concentration of PPi. The black line is the non-linear fitting curve between **1**-Al^{3+} and PPi. Association constant (*K*) of **1**-Al^{3+} with PPi was calculated by the non-linear least square curve fitting.

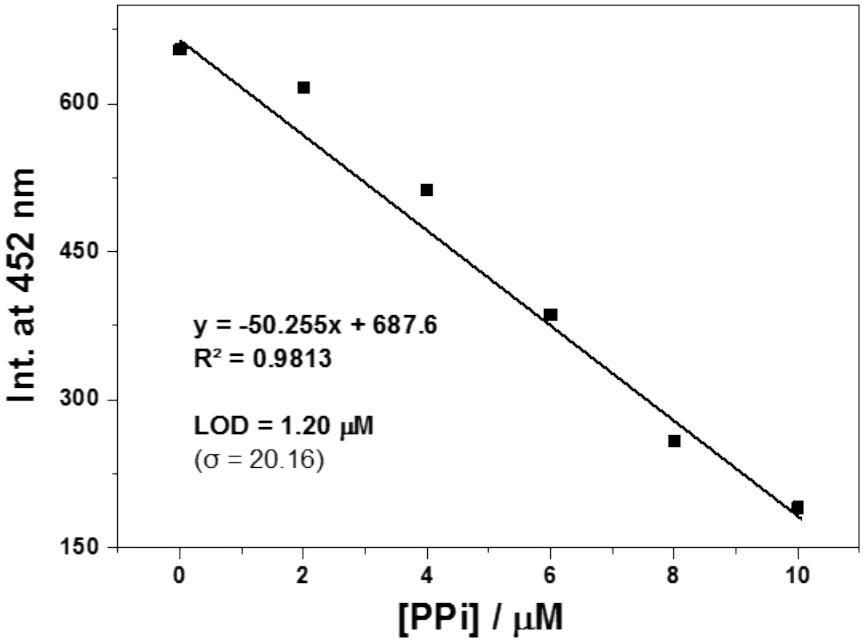

Figure S13. Determination of the limit of detection based on change in the ratio (fluorescence intensity at 452 nm) of **1**-Al^{3+} complex (1 μM) with PPi.

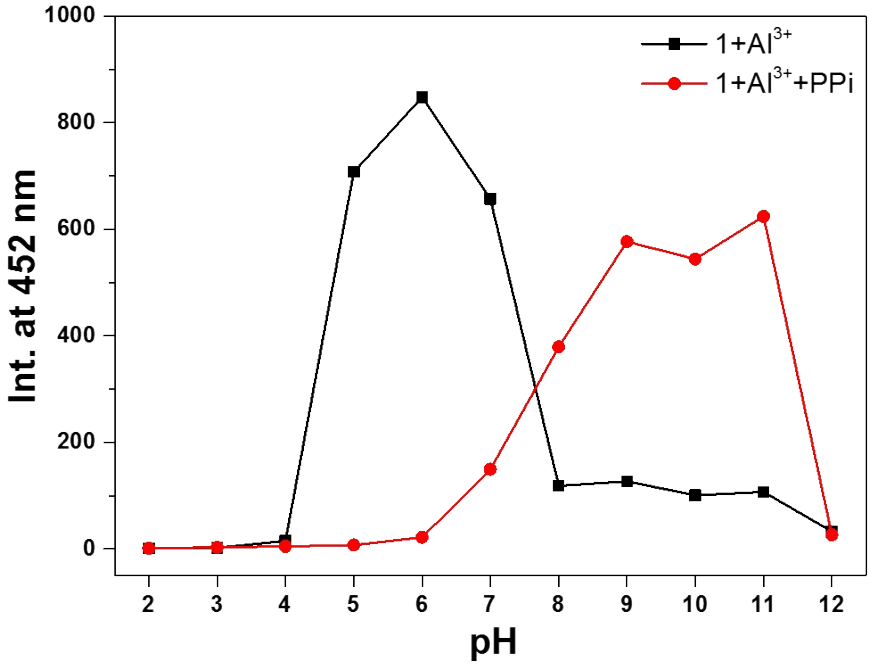

Figure S14. Fluorescence intensities (at 452 nm) of **1**-Al^{3+} and **1**-Al^{3+} + PPi ([**1**-Al^{3+}] = 1 μM) after addition of 24 equiv of PPi at various ranges of pH in bis-tris buffer solution.

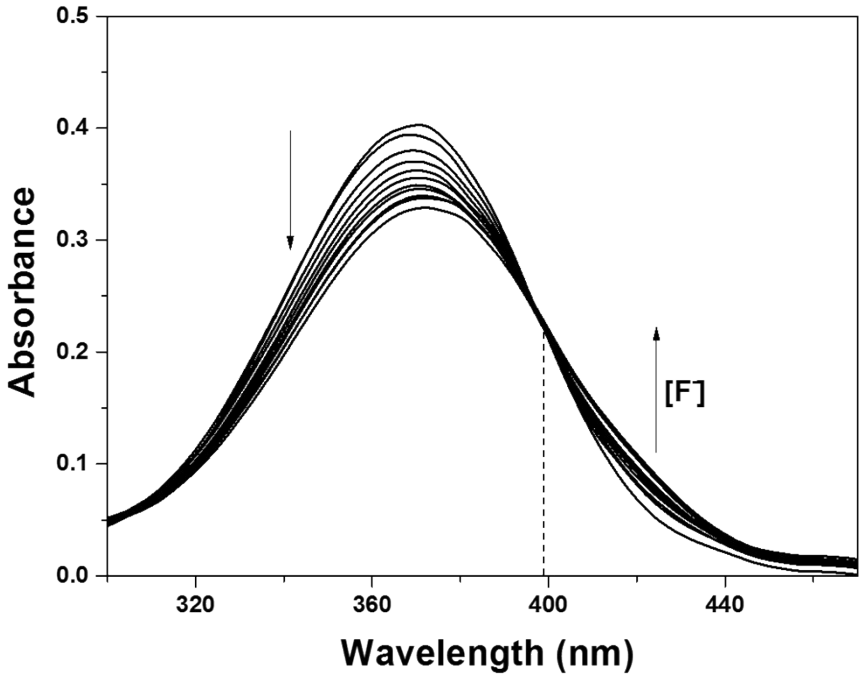

Figure S15. UV-vis titration of **1** (10 μM) with F^- (up to 50 equiv) in bis-tris buffer solution at room temperature.

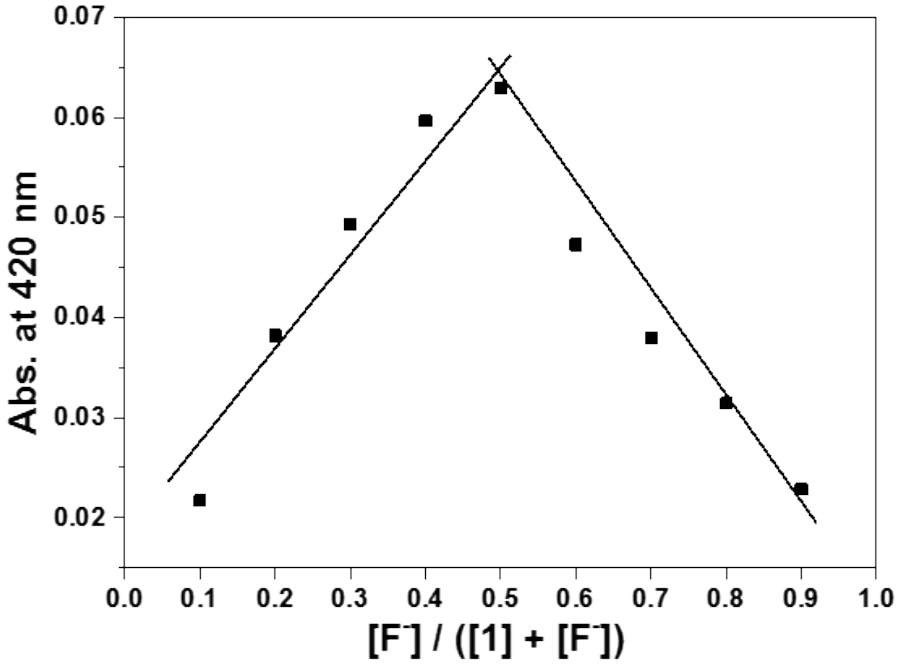

Figure S16. Job plot for the binding of **1** with F^-. Absorbtion at 420 nm was plotted as a function of the molar ratio $[F^-] / ([\mathbf{1}] + [F^-])$. The total concentration of **1** with F^- was 200 μM.

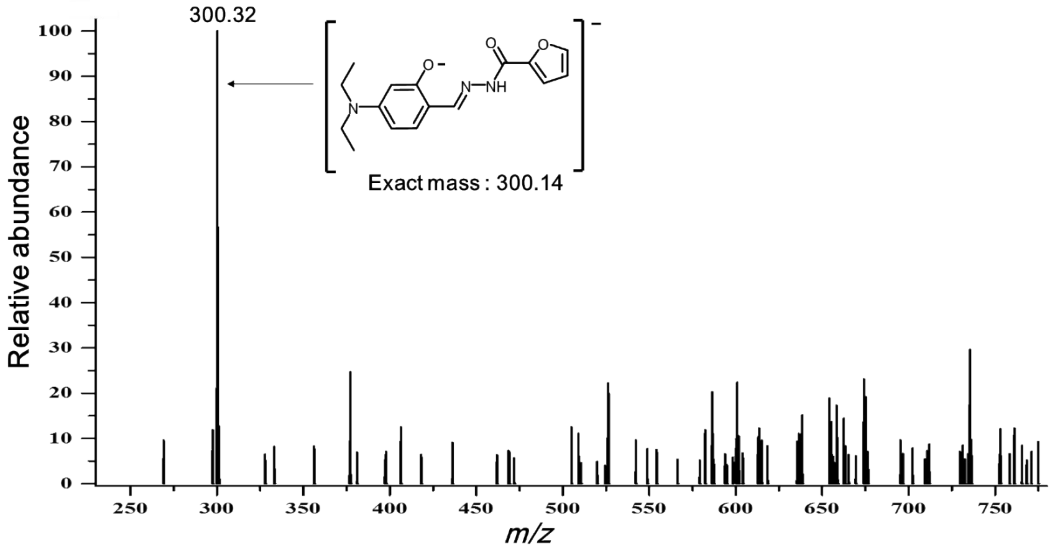

Figure S17. Negative-ion ESI-mass spectrum of **1** (100 μM) upon addition of 2 equiv of F^-.

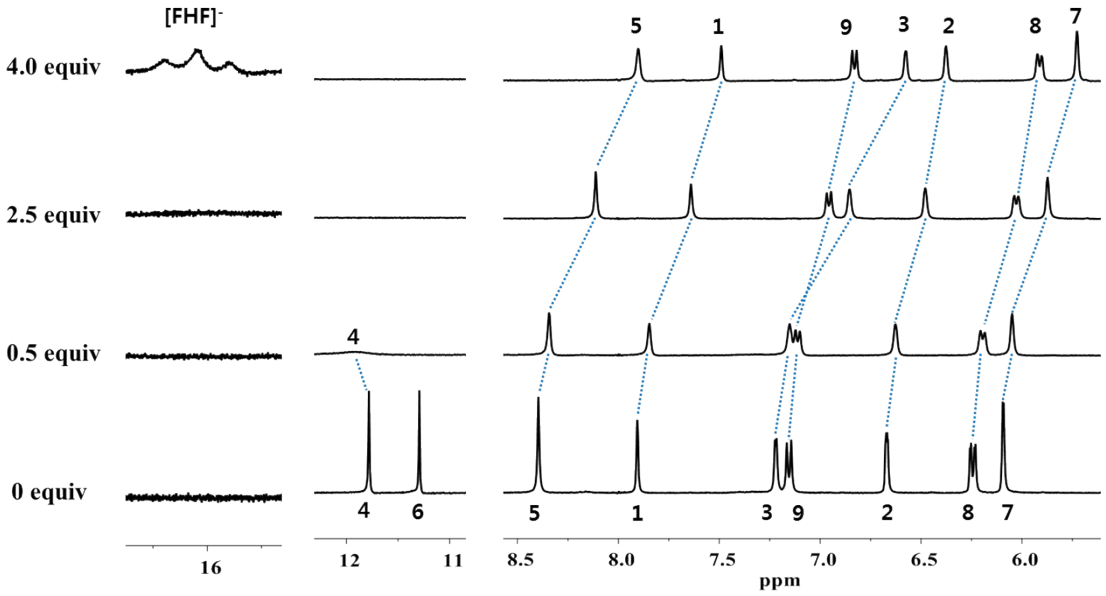

Figure S18. ^{1}H NMR titrations of **1** with F^{-}.

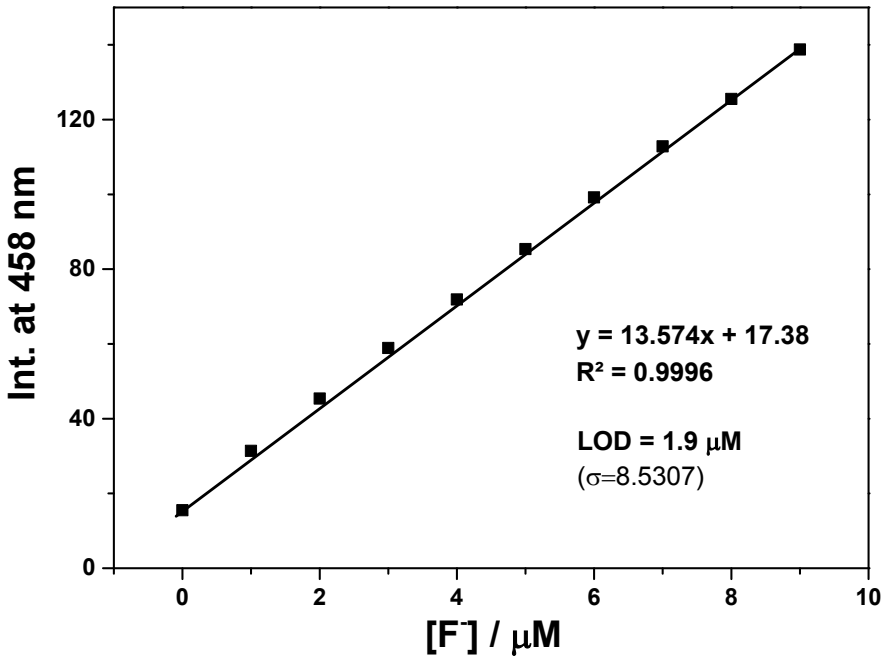

Figure S19. Determination of the limit of detection based on change in the ratio (fluorescence intensity at 458 nm) of **1** (10 μM) with F^-. [**1**] = 10 μM and [F^-] = 0-9 μM

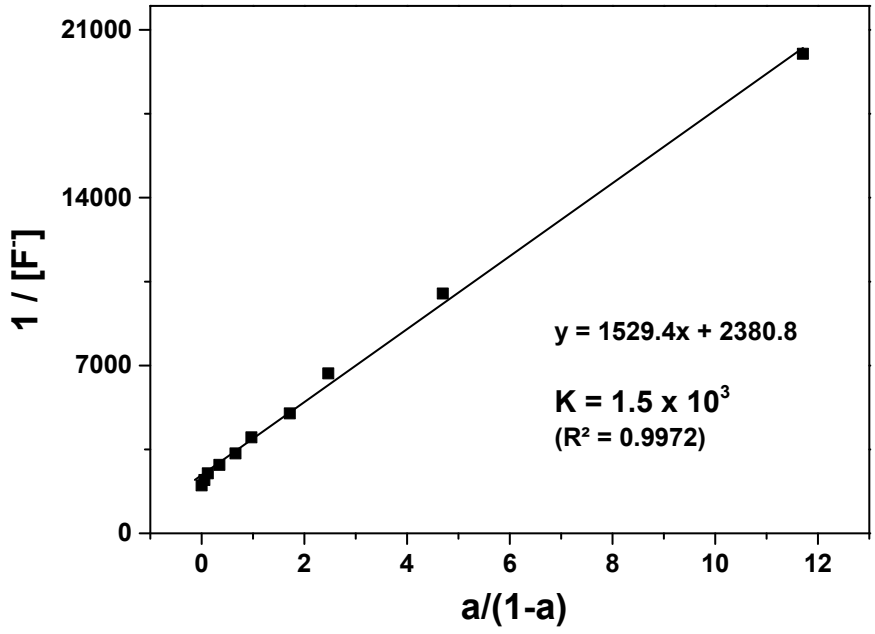

Figure S20. Li's plot (Intensity at 458 nm) of **1**, assuming 1:1 stoichiometry for association between **1** and F^-.

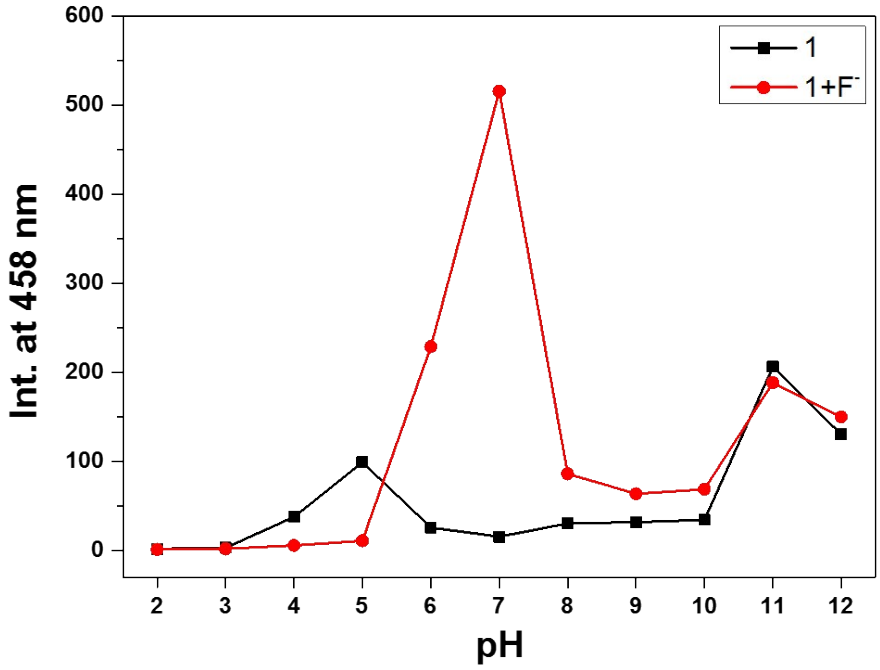

Figure S21. Fluorescence intensities (at 458 nm) of **1** and **1**-F^- ([**1**] = 10 μM) after addition of 50 equiv of F^- at various ranges of pH in bis-tris buffer solution.

(a)

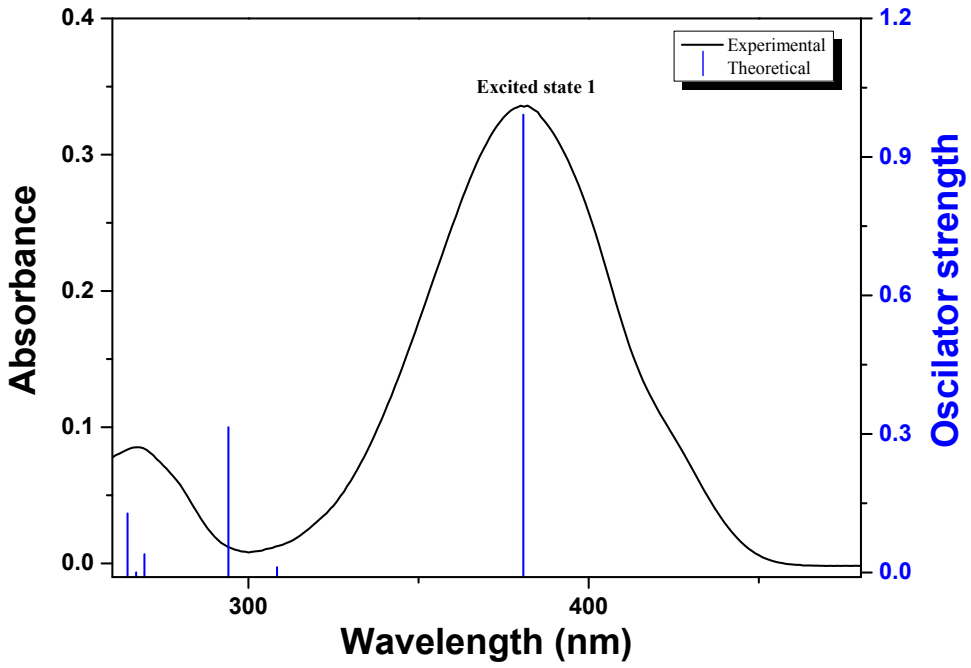

(b)

Excited state 1	Wavelength	Percent (%)	Character	Oscillator strength
H → L	380.76 nm	99%	ICT	0.9914

Fig. S22. (a) The theoretical excitation energies and the experimental UV-vis spectrum of **1**. (b) The major electronic transition energies and molecular orbital contributions for **1** (H = HOMO and L = LUMO).

(a)

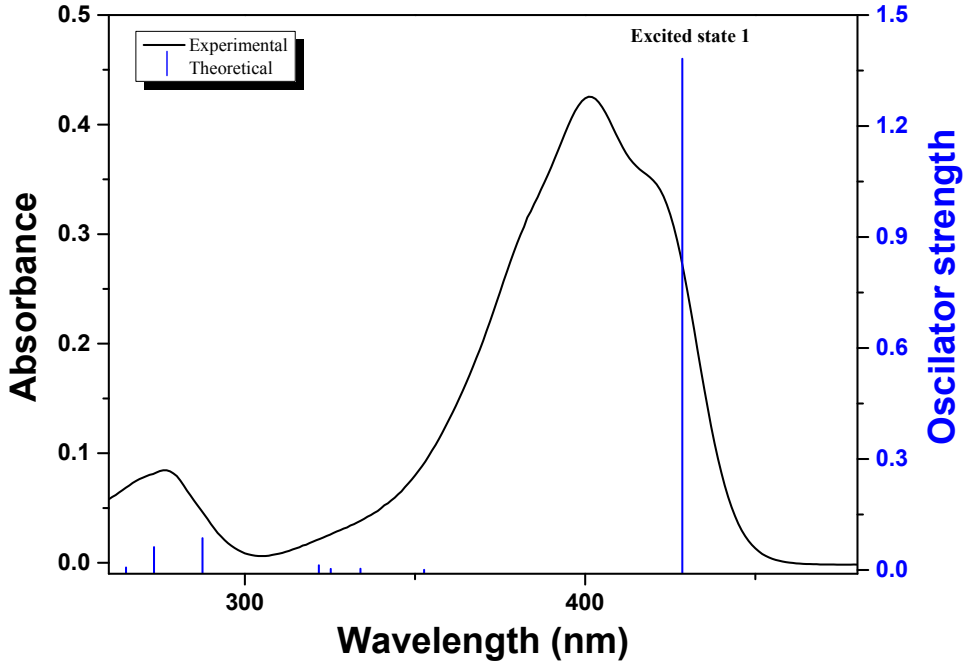

(b)

Excited State 1	Wavelength	percent (%)	Character	Oscillator strength
H → L	428.55	99%	ICT	1.3816

Fig. S23. (a) The theoretical excitation energies and the experimental UV-vis spectrum of **1**-Al^{3+}. (b) The major electronic transition energies and molecular orbital contributions for **1**-Al^{3+} (H = HOMO and L = LUMO).

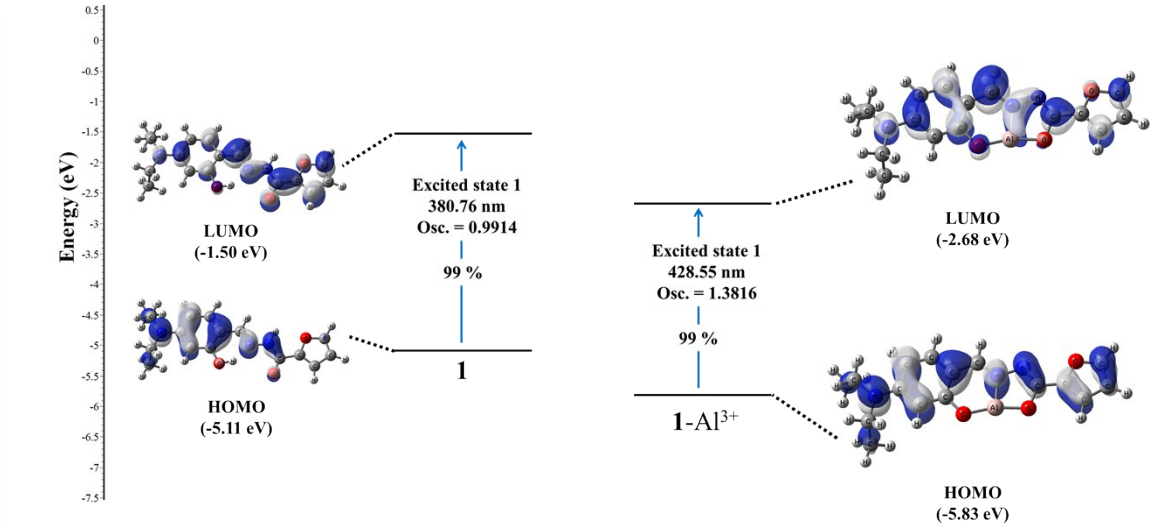

Fig. S24. Molecular orbital diagrams and the excitation energies of **1** and **1**-Al^{3+}.

(a)

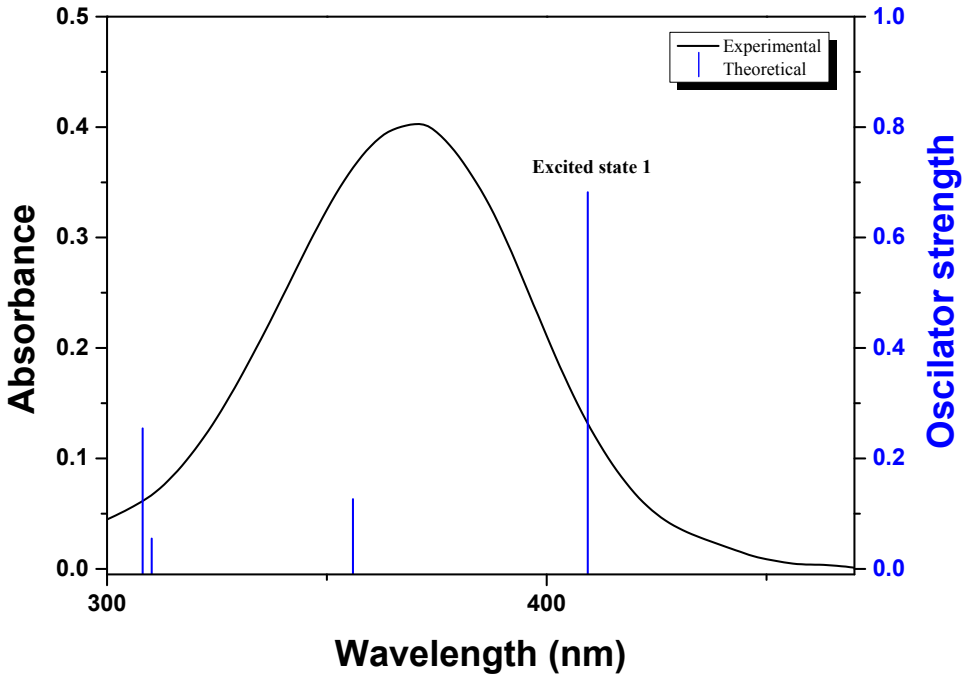

(b)

Excited State 1	Wavelength	percent (%)	Character	Oscillator strength
H → L	409.33 nm	98%	ICT	0.6819

Fig. S25. (a) The theoretical excitation energies and the experimental UV-vis spectrum of **1**-F^-. (b) The major electronic transition energies and molecular orbital contributions for **1**-F^- (H = HOMO and L = LUMO).

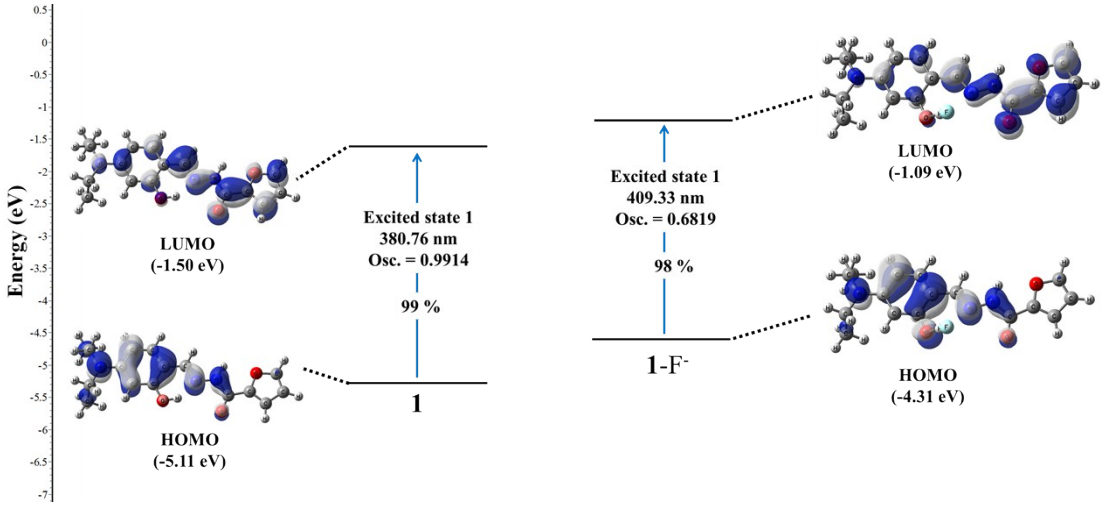

Fig. S26. Molecular orbital diagrams and the excitation energies of **1** and **1**-F^-.